Article

Fabrication of Asymmetric Supercapacitors (AC@GQDs//AC) with High Electrochemical Performance Utilizing Activated Carbon and Graphene Quantum Dots

Huda S. AlSalem, Khadijah Mohammed Saleh Katubi, Mona Saad Binkadem, Soha Talal Al-Goul, and Ahmed M. Wahba*

Read Online

ACCESS | Metrics & More | Article Recommendations

ABSTRACT: Sugar cane bagasse stands as a prevalent and abundant form of solid agricultural waste, making it a prime candidate for innovative utilization. Harnessing its potential, we embarked on a groundbreaking endeavor to evaluate the sustainability of a molasses-based hydrothermal process to produce graphene quantum dots (GQDs). This pioneering initiative promises remarkable environmental benefits and holds immense economic potential. Embedding crystalline GQDs in activated carbon (AC) boost electrochemical efficiency by enhancing charge-transfer and ion migration kinetics. Optical, structural, and morphological evaluations were used to confirm the formation of GQDs. Transmission electron microscopy (TEM) investigation showed the size, shape, and fact that GQDs were monodispersed, and X-ray diffraction and Fourier transform infrared determined the structure of GQDs. The electrodes with negative (AC) and positive (AC@GQDs) polarity demonstrate a considerable specific capacitance of 220 and 265 F g^{-1}, respectively, when measured at 0.5 A g^{-1}. Additionally, these electrodes exhibit high-rate capabilities of 165 and 230 F g^{-1} when measured at 5 A g^{-1}, as determined by galvanostatic charge−discharge techniques. The supercapacitor device comprising asymmetric AC//AC@GQDs exhibits a specific capacitance of 118 F g^{-1}. Furthermore, the asymmetric device exhibits exceptional cycling behavior, with an impressive 92% capacitance retention even after undergoing 10,000 cycles. This remarkable performance underscores the immense potential of both the negative and positive electrodes for real-world supercapacitor applications. Such findings pave the way for promising advancements in the field and offer exciting prospects for practical utilization.
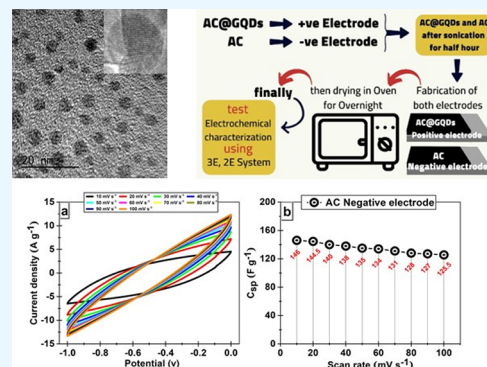
1. INTRODUCTION

The electrochemical double-layer capacitor (EDLC) effect or surface-fast redox reactions are two ways that high-capacity electrochemical capacitors (supercapacitors) store energy.[1] These materials have recently become significant energy storage devices due to quick charging/discharging, strong power, and good cycle stability.[2] Moreover, discovering innovative nanoscale electrode materials and better device manufacturing processes have significantly boosted their energy densities.[3] For these reasons, high-power applications often employ a combination of supercapacitor and battery or fuel-cell technology.[4]

Pseudocapacitors provide less power density and a shorter cycle life.[5] Asymmetric supercapacitors, also known as supercapattery devices, combine the benefits of EDLCs and pseudocapacitors to compensate for their shortcomings.[6] It functions and performs similarly to a battery-supercapacitor hybrid. Compared to standalone supercapacitors and battery systems, this hybrid system's energy and power densities are considered remarkable, having a good position in energy

storage.[7,8] The electrode manufacturing techniques greatly influence the storage characteristics of supercapattery devices.[9]

Activated carbons (ACs) are one of the common electrode substances for supercapacitors owing to their cheap and broad surface area.[10−12] However, AC often has a poor energy density and low capacitance, severely limiting their practical uses of supercapacitors.[13] Numerous studies have already been done to enhance the capacitance of AC, especially by expanding their volume-to-surface ratio using the electric double-layer energy storage process.[10,14,15] By disrupting the conductive networks, the porosity construction diminishes the electrical conductivity of the AC dramatically. Moreover, deep

and branching micropores have a restricted capacity for electrolyte ion transit and storage.[16,17] Challenges lead to limited surface area utilization, insufficient capacitance, poor rate performance, and delayed electrochemical kinetics.[18,19] Several efforts have been undertaken to address these issues by combining AC with other carbon materials that conduct electricity, like graphene nanosheets or carbon nanotubes.[20−22] Unfortunately, due to their huge sizes and low compatibility, these conductive nanocarbons cannot thoroughly combine at the molecular level with porous carbons to make conductive networks, hindering their performance.[23]

In contrast to graphene or carbon nanotubes, graphene quantum dots (GQDs) offer a distinct advantage in terms of their exceptional crystallinity and zero-dimensional nature.[24,25] These remarkable nanostructures have recently garnered significant attention for their ability to serve as high-performance materials for energy storage, owing to their ultrafine particle sizes and unique physicochemical properties.[26−28] By enhancing the electrochemical kinetics and conductivity of other active materials, GQDs have revolutionized the field. Consequently, various composites, such as GQD/MnO$_2$,[29] GQD/halloysite nanotube,[30] GQD/NiCo$_2$O$_4$,[28,31] and GQD/polypyrrole,[32] have been developed to yield supercapacitor electrodes with exceptional performance characteristics. These advancements hold tremendous promise for the development of next-generation energy storage systems.

On the other hand, the world wants an innovative biomass material sector to alleviate energy issues and environmental issues. Biorefinery researchers have worked hard to generate high-value materials.[33−35] Bagasse from sugar cane is a highly valuable byproduct of agriculture. It is one of the world's most prolific agricultural wastes and benefits industrial production with its high output, focused generating area, low price, and steady and unified qualities. Sugar cane bagasse is composed of 38−59% lignocellulose, 18−26% hemicellulose, and 16−25% lignin.[36−38] It has rich oxygen and carbon components and fewer ash concentrations than other agricultural wastes, which makes it an intriguing carbon material source. Therefore, using very valuable sugar cane bagasse for energy production and storage still needs to be explored. Since it contains a lot of carbon and heteroatoms, this biomass material has occupied a significant position.[39] However, there is a lack of performed in-depth investigations on the makeup and structure of biomass quantum dots and their production mechanism, which has hampered the examination of the GQDs production.[40,41]

Here, the one-step hydrothermal process disclosed a green method for creating GQDs from molasses. Once the GQDs were prepared, the structural and morphological characteristics were investigated using UV−vis, photoluminescence (PL), transmission electron microscopy (TEM), X-ray diffraction (XRD), X-ray photoelectron spectroscopy, Brunauer−Emmett−Teller, etc. Asymmetric supercapacitor formation with high electrochemical achievement using AC and GQDs was carefully examined in this work. This study will significantly affect how sugar cane bagasse can be used overall and give a theoretical foundation for making more trustworthy products.[35]

2. EXPERIMENTAL SECTION

2.1. Materials. The Sugar cane molasses sample with brix (%) 79.4, polarity (%) 37.4, water content (%) 25.1, and the determined ash ratio was 4.6% without any dilution. Sugar cane bagasse was obtained from the United Sugar Company, Jeddah, Saudi Arabia. Carbon black acetylene (CB), N-methyl pyrrolidone (NMP), and AC were supported by LobaChemie (India). 44080 (vinylidene fluoride) was endorsed by Alfa Aesar (Germany). Other noticed chemicals were used as is without pretreatment.

2.2. Preparation of GQDs. The hydrothermal process was the standard for preparing GQDs. A homogeneous aqueous solution was prepared by diluting 5 mL of cane molasses in 100 mL of pure water, followed by ultrasonication for 20 min and centrifugation. The next step involved transferring 70 mL of the cane molasses supernatant into a 150 mL autoclave reactor and heating it at 200 °C for 10 h. After the reactor cooled to room temperature, the carbon slag residue was separated from the primary liquid by filtration through the Whatman filter paper (20 μm) to obtain GQDs. The direct liquid of the GQDs was then diluted with deionized water 30-fold to obtain the GQDs solution.

2.3. Characterization. The Systronics UV−vis Spectrophotometer-117 was used to study how GQDs absorb UV to confirm its formation; the UV−vis was made in the range of 200−800 cm^{-1}.

In an aqueous solution, a photoluminescent setup (Hitachi F-7000) was used to record the photoluminescent spectra.

XRD (Bruker), Advance D8, was used to define the crystal evidence of GQD with Cu-kα radiation (0.15406 nm) using an accelerating voltage of 40 kV.

The shape and structure of the samples were studied with TEM (JEOL-2100F).

Drawell DTR3010 Raman Spectroscopy Portable Raman Spectrometer was used to study the vibration mode of GQD.

2.4. Preparation of the AC Negative Electrode. First, a substrate made of a nickel sheet is prepared to be thoroughly cleaned in a H$_2$SO$_4$ solution with a concentration of 6 mL and then in deionized water. Second, the homogeneous slurry is prepared by the following steps: 80% AC, 10% CB acetylene, and 10% PVDF in a solvent of NMP (N-methyl-2-pyrrolidone) with a concentration of 0.3 mL. Finally, the estimated mass of the cathode (3.1 mg) was dried at 90 °C for five hrs. Similarly, the positive electrode AC@GQDs were fabricated with the same active mass as a positive electrode, and the process is illustrated in Scheme 1.

Scheme 1. Simple Chart for the Preparation of AC and AC@GQDs Electrodes
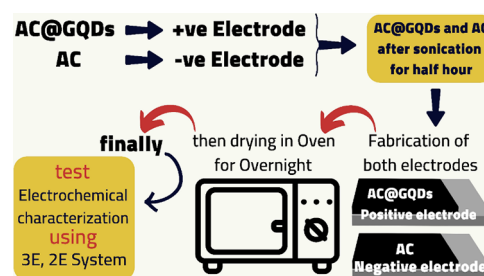
2.5. Electrochemical Measurements. For the −ve (AC) and +ve (AC@GQDs) electrodes with the three-electrode system, the three techniques of galvanostatic charge−discharge (GCD), electrochemical impedance spectroscopy (EIS), and cyclic voltammetry (CV) were applied in 1 M Na$_2$SO$_4$ aqueous solution.
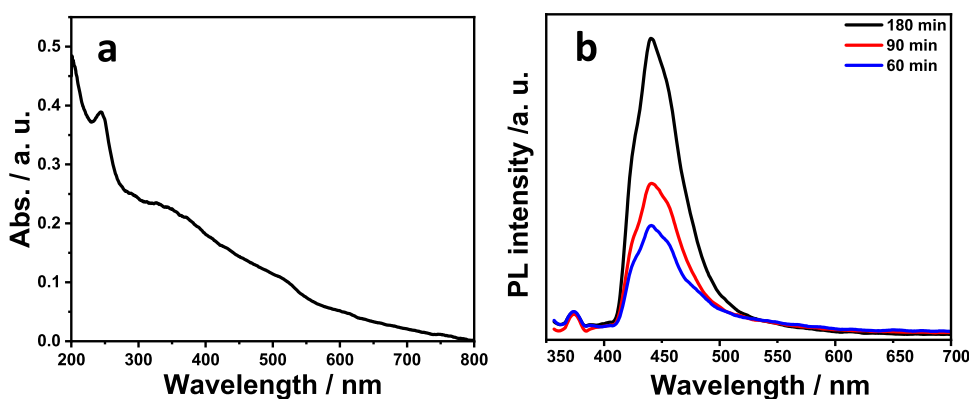
Figure 1. (a) UV−vis and (b) PL intensities of GQDs from cane molasses.

Platinum wire was used as the counter electrode, Ag/AgCl (KCl saturated) was used as a reference electrode, and AC@CdO nanomaterial was used as a working electrode. At varied scan rates, from 10 to 100 mV s^{-1}, the cyclic voltammograms were taken at different voltages (0−1 V). GCD investigations were conducted at various specific currents (0.5−4.5 A g^{-1}). Additionally, with a 10 mV amplitude, the EIS was computed in the frequency range of 100 kHz to 10 MHz.

The specific capacitance (C_{sp}, F g^{-1}) was computed from the GCD and CV measurements.[42] The specific energy (SE, Wh kg^{-1}), specific power (W kg^{-1}), and Coulombic efficiency (η%) were computed from GCD and are measured according to those reported elsewhere.[43]

3. RESULTS AND DISCUSSION

3.1. Fabricated GQDs Characteristics. *3.1.1. Optical Properties.* The UV−vis spectra of GQDs are shown in Figure
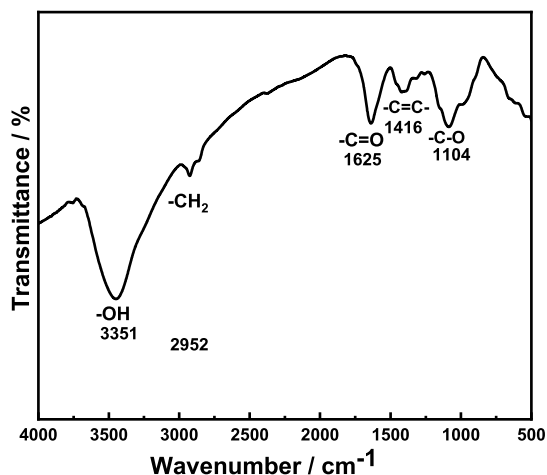

Figure 2. FTIR characteristics for GQD.

1a. Notably, even after an extended period at room temperature, the as-prepared GQDs exhibit a uniform phase without any observable precipitation. A key characteristic of GQDs is their absorption peak at 235 nm, which can be attributed to the transition of aromatic sp^2 domains ($\pi \rightarrow \pi^*$).[44] Additionally, the absorption peak at 360 nm in the GQDs can be attributed to the transitions of C=O (n $\rightarrow \pi^*$).[45] These absorption features provide valuable insights into the unique optical properties and molecular structure of GQDs.

The PL intensity, when excited at 365 nm, reveals intriguing excitation-dependent behavior at different time intervals. Notably, a distinct peak is observed at a wavelength of 440.4 nm, as illustrated in Figure 1b, which corresponds to excitations involving sp^2 and sp^3 hybridized carbon atoms. This phenomenon can be attributed to the presence of localized π electrons in the −C=C− bonds, leading to UV absorption and subsequent relaxation through vibrational processes and interband transitions of excited electrons. As a result, the excited GQDs emit a vibrant blue-green luminescence, which can be ascribed to the combined effects of their size and surface functional moieties. This specific PL emission serves as a primary distinguishing characteristic of GQDs, setting them apart from previously reported carbon dots.[45] These findings shed light on the unique optical properties and potential applications of GQDs in various fields, such as optoelectronics and bioimaging.

3.1.2. FTIR. The functional groups are investigated by using Fourier transform infrared (FTIR) spectroscopy (Figure 2). The absorption peak at 3351 cm^{-1} is assigned to the stretching vibrations of the O−H moiety's stretching vibrations. A peak at 1625 cm^{-1} confirms the C=O moiety, and the C−O stretching refers to the epoxy moiety and depicts a peak at 1104 cm^{-1}.[46] The peaks at 2952 and 2336 cm^{-1} are owing to C−H and O=C=O groups, respectively.[46] Throughout oxidation, oxygen-containing moieties were added to the margins and basal plane. The GQDs feature numerous oxygen-bearing functional moieties mainly produced as C−O−C, C−OH, C=O, and −COOH, ensuring their excellent dispersibility, high chemical reactivity, and strong compatibility, as revealed by FTIR analysis.

3.1.3. XRD Crystallographic Analysis. Figure 3a shows the GQDs crystallographic evaluation using XRD. The XRD displays a broad peak at 25.6 Å that is associated with the (002) peak, which conforms to JCPDS Card no. 75-0444; likewise, the intense peak of GQDs is attributed to the eminent crystallinity with the graphitic structure,[47] implying that sugar cane produced GQD structures via the hydrothermal technique.

The Raman spectrum (Figure 3b) exhibits two prominent bands, D and G, at 1345 and 1581 cm^{-1}, respectively. The peak at 1345 cm^{-1} can be unequivocally ascribed to the D band, primarily arising from the vibrations of carbon atoms resulting from structural defects. Conversely, the peak at 1581 cm^{-1}, corresponding to the G band, originates from in-plane sp^2 bonded carbon atoms vibrations. The intensity ratio of the
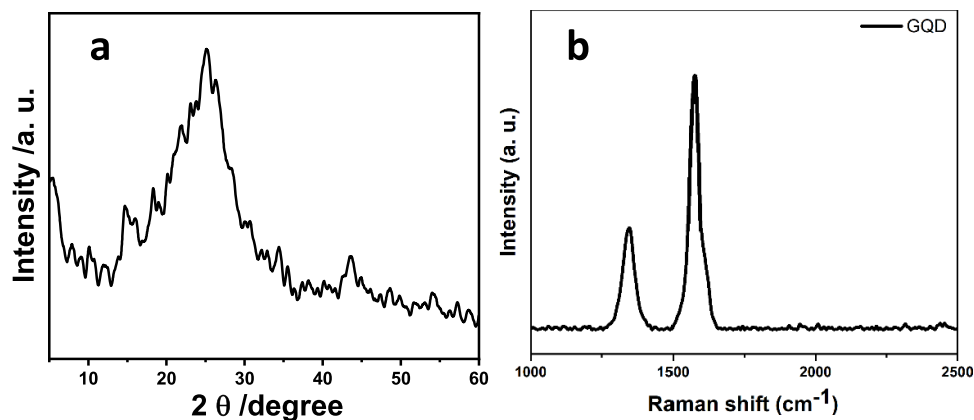
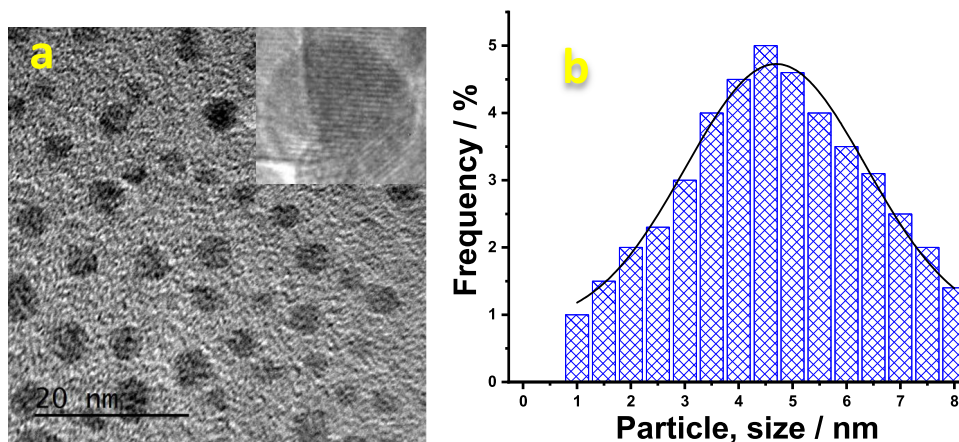**Figure 3.** (a) XRD crystal evidence and (b) Raman spectra of GQD.

Figure 4. (a) TEM configuration (inside HRTEM) and (b) DLS of GQDs.

disordered D band to the crystalline G band, I_D/I_G, is determined to be approximately 0.22.

3.1.4. Morphology Study. The morphology and internal structure of GQDs were meticulously examined by using TEM analysis. As depicted in Figure 4, the TEM image showcases the monodisperse nature of GQDs, which exhibit a nearly spherical shape without any noticeable agglomeration. The distribution of GQD diameters reveals the presence of varying sizes, with approximately 45% of particles falling within the range 6−8 nm, 20% within the range 11−17 nm, and around 35% exhibiting sizes smaller than 6 nm. Furthermore, the size distribution analysis (Figure 4b) indicates that the mean size of GQDs falls within the range of 3.34 ± 0.28 nm.[48] These findings provide valuable insights into the uniformity and size characteristics of GQDs, contributing to a comprehensive understanding of their structural properties.

3.2. Electrochemical Studies (AC Negative Electrode). In a three-electrode arrangement, the performances of the AC were examined using CV, GCD, and EIS techniques.[49] The negative electrode materials' CV curves (AC) demonstrated satisfactory capacitive behaviors over a range of scan rates, from 10 to 100 mV s^{-1} (Figure 5a). The C_{sp} of the AC electrode possessed 146 and 125.5 F g^{-1} depicted in Figure 5b, which was obtained at 10 and 100 mV s^{-1}, respectively. Figure 5c displays the GCD curves for an AC negative electrode up to 5 A g^{-1}.[50] The AC electrode's extended discharge time in the GCD curves suggested that it had a greater capacity for storing charges. According to Figure 5d, the AC electrode had specific

capacities regardless of current densities of 220, 190.5, and 165 F g^{-1} at 0.5, 2.5, and 5 A g^{-1}, respectively. The Coulombic efficiency of the negative electrode was calculated after knowing the shape of the GCD curves and their specific capacitance, where the values of the Coulombic efficiency were 76 and 100% at 0.5 and 5 A g^{-1} (Figure 5e). The EIS technique was used with an open-circuit potential to examine the fundamental behavior of the AC electrode.[51] According to calculations, the negative electrode's equivalent series resistance (ESR) is 3.8 Ω, which is depicted in Figure 5f.

3.3. Electrochemical Studies (AC@GQDs Positive Nanoelectrode). The electrochemical efficiency of the positive nanoelectrode (AC@GQDs) in a three-electrode configuration was examined using CV, GCD, and EIS techniques, whereas Figure 6a illustrates the positive AC@GQD nanoelectrode CV curves, which exhibit good capacitive characteristics at range (10−100 mV s^{-1}). The AC@GQDs positive nanoelectrode exhibited specific capacities of 158 F g^{-1} (10 mV s^{-1}) and 121 F g^{-1} (100 mV s^{-1}) displayed in Figure 6b. The GCD curves of positive nanoelectrode are illustrated in Figure 6c, and the current density is from 0.5 to 5 A g^{-1}. Larger charge storage capacity is indicated by the longer discharge time in the GCD curves of the AC@GQDs positive nanoelectrode.[52] The C_{sp} values were 265, 238, and 230 F g^{-1} at 0.5, 2.5, and 5 A g^{-1}, respectively, for the AC@GQDs electrode depicted in Figure 6d. The Coulombic efficiencies of an AC@GQDs positive nanoelectrode were 80, 98, and 100% at 0.5, 2.5, and 5 A g^{-1}, respectively, as shown in Figure 6e. As
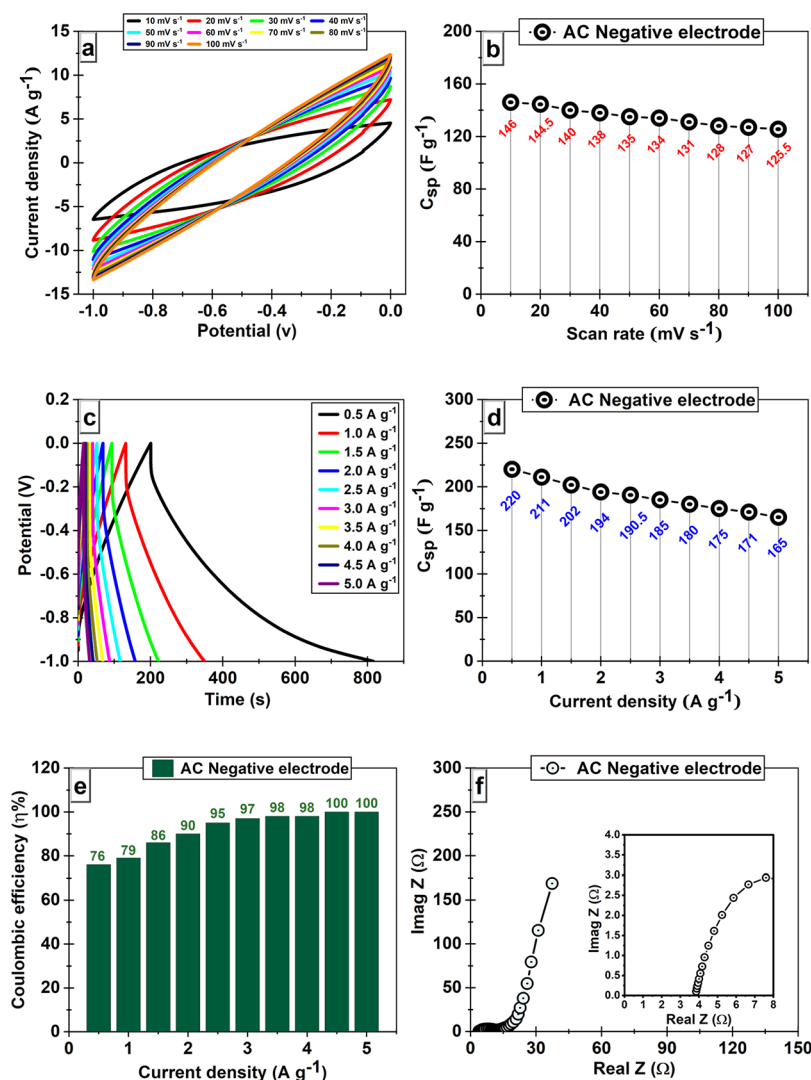
Figure 5. (a) CV curves, (b) calculated C_{sp}, (c) GCD curves, (d) C_{sp} at range (0.5−5 A g^{-1}) for AC, (e) η% for AC, and (f) Nyquist plots for the AC negative electrode.

depicted in Figure 6f, the EIS technique was used to analyze the fundamental behavior of the positive nanoelectrode, including its specific capacitance, charge transfer resistance, and ESR. Calculations show that the ESR of the AC@GQDs nanoelectrode is 3.15 Ω.

3.4. AC@GQDs//AC Asymmetric Supercapacitor Device. To investigate the electrochemical behavior of the asymmetric AC@GQDs//AC devices, CV was employed by using a two-electrode configuration. The CV curves of the asymmetric device, as shown in Figure 7a, were recorded at scan rates of 10 mV s^{-1}, with a voltage range extending up to 1.8 V. This experimental setup allowed for a comprehensive analysis of the device's electrochemical performance and provided valuable insights into its charge storage capabilities and stability under varying scan rates and voltage ranges.[53] During different scan rates, Figure 7b shows the CV curve of the AC@GQDs//AC asymmetric device, which indicates good capacitive characteristics and, consequently, the significant activity of asymmetric supercapacitor materials. CV curves were integrated to calculate the C_{sp} values for the AC@GQDs//AC device, which were determined to be 110 and 80 F g^{-1} at the lowest (10 mV s^{-1}) and highest (100 mV s^{-1}) scan rate (Figure 7c). At (1 to 1.8 V) of the voltage range, Figure 7d

illustrates the asymmetric AC@GQDs//AC device GCD curves at 1 A g^{-1}. Furthermore, Figure 7e shows the GCD curves of the asymmetric AC@GQDs/AC device at 1 to 5.5 A g^{-1} of current density. The asymmetric AC@GQDs//AC device (Figure 7f) at a potential window of 1.8 V exhibits suitable specific capacitance of 118 and 76 F g^{-1} at 1 and 5.5 A g^{-1} current densities. The AC@GQDs//AC asymmetric device's Coulombic efficiency was determined, and the results are presented in Figure 7g. The Coulombic efficiencies were 85 and 99% at 1 and 5.5 A g^{-1}, respectively. Due to the good C_{sp} of the AC@GQDs//AC device, it achieved a very good energy density estimated at 50.5 Wh kg^{-1} at 1085 W kg^{-1} (very large power density) as shown in Figure 7h.[54] Finally, Figure 7i displays the asymmetric AC@GQDs//AC device, which achieved an excellent result of 96.5% with η of 98 and 93% with η of 99% after 5000 and 10,000 cycles of capacitance retention and Coulombic efficiency. Table 1 presents a comparison between our system vs asymmetric super-capacitors.
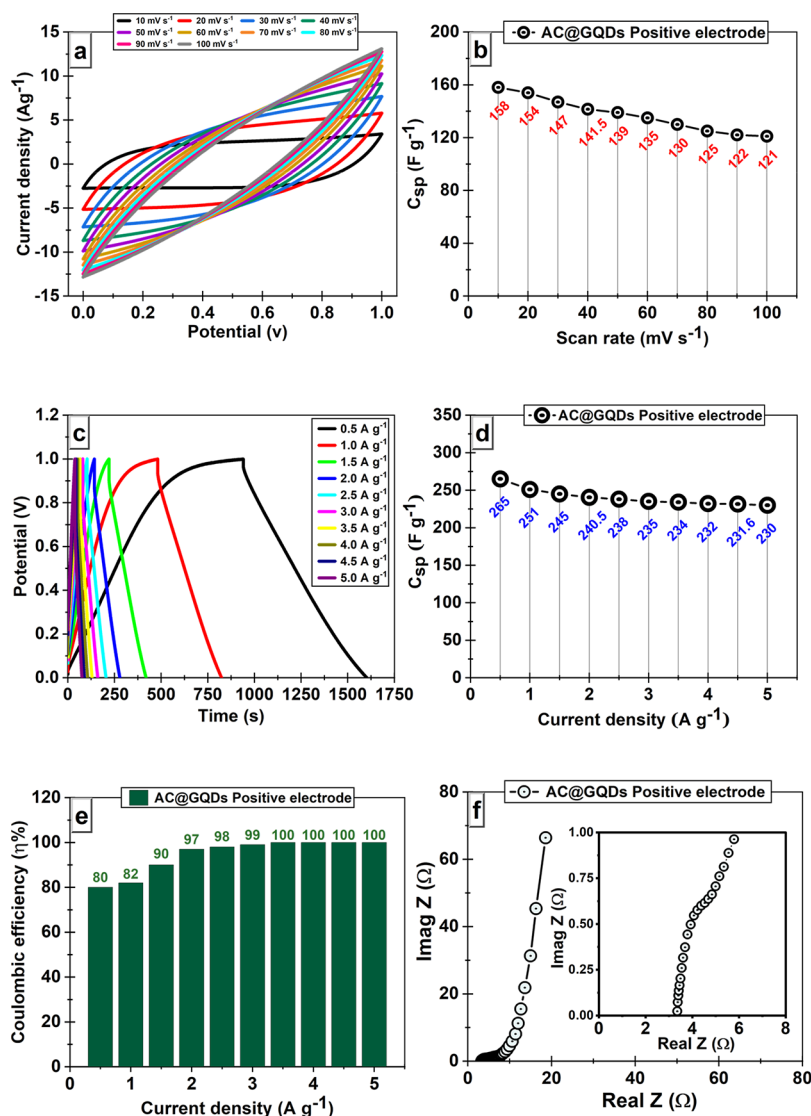
Figure 6. (a) CV curves, (b) calculated C_{sp}, (c) GCD curves, (d) C_{sp} at range (0.5–5 A g^{-1}) for AC, (e) η% for AC, and (f) Nyquist plots for the AC@GQDs positive electrode.

Table 1. Asymmetric Supercapacitors vs Our Constructed AC@GQDs//AC Device

design	type	electrolyte	voltage (V)	C_{sp} (F g^{-1})	SE (Wh kg^{-1})	retention	ref
BiFeO$_3$/g-CN/NGQDs //AC	asymmetric	2 M KOH	1.4	195	53.1	87% 3k cycle	[55]
N-GQD/H-NiCo-LDH//AC	asymmetric	2 M KOH	1.6	146	52.1	80.5% 5k cycle	[56]
MnO$_2$//AC-MnO$_2$	asymmetric	1 M KOH	1.2	83.33	42.2		[57]
Ni$_3$S$_4$ QDs@G/CNTs //AC	asymmetric	6 M KOH	1.6		50	80% 4k cycle	[58]
AC@GQDs//AC	asymmetric	1 M Na$_2$SO$_4$	1.8	118	50.5	92% 10k cycle	this work

4. CONCLUSIONS

In pursuit of an economical and environmentally friendly solution for recycling agricultural waste, a cost-effective and sustainable system was developed. This innovative approach involved the synthesis of GQDs from biodegradable molasses using a simple one-step hydrothermal method. Extensive investigations explored the optical, structural, and morphological properties of the as-prepared GQDs. The analysis revealed that the GQDs possessed a mean size smaller than 6 nm, with a distinct broad peak detected at approximately 25.6 Å, providing compelling evidence of the existence of GQDs in the sample. These findings shed light on the unique characteristics and potential applications of the synthesized GQDs, further highlighting their significance in the field of sustainable materials research.

Supercapacitors' negative and positive electrodes were made of AC and GQDs, respectively. These electrode materials demonstrated stable cyclability at high rates, which verified AC and AC@GQDs as potential electrode materials for supercapacitors. AC@GQDs and AC electrodes display specific 265 and 220 F g^{-1} capacitances derived from the GCD curves.

The AC@GQDs/AC device demonstrated exceptional electrochemical performance at a potential window of 1.8 V. Specifically, it exhibited an ultrahigh specific capacity of 118 F g^{-1}, a high energy density of 50.5 Wh kg^{-1}, a maximum power
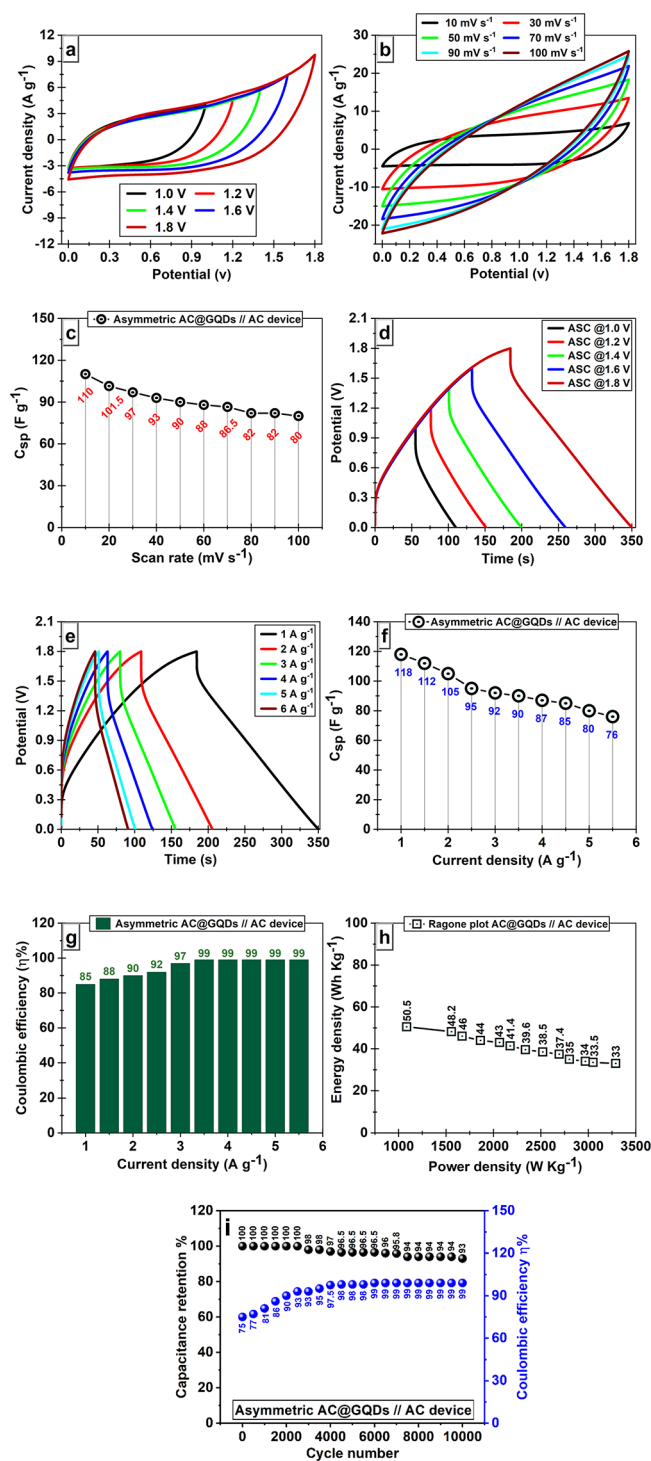
Figure 7. (a) CV at 50 mV s^{-1}, (b) CV, (c) C_{sp}, (d) GCD curves, (e) GCD at various current density, (f) C_{sp} at range 1 to 5.5 A g^{-1}, (g) $\eta\%$, (h) Ragone plot, and (i) capacitance retention and Coulombic efficiency at 5.5 A g^{-1} for the AC@GQDs//AC device.

density of 1085 W kg^{-1} at 1 A g^{-1}, and remarkably stable cycling with 93% capacitance retention following 10,000 cycles.

ASSOCIATED CONTENT

Data Availability Statement

The author confirms that the data supporting this study are available within the article.

AUTHOR INFORMATION

Corresponding Author

Ahmed M. Wahba − *Department of Basic Science, Higher Institute of Engineering and Technology (HIET), El-Mahalla 12311, Egypt;* orcid.org/0000-0002-6771-6973; Email: Ahmed.m.wahba1988@gmail.com

Authors

Huda S. AlSalem − *Department of Chemistry, College of Science, Princess Nourah bint Abdulrahman University, Riyadh 11671, Saudi Arabia*

Khadijah Mohammed Saleh Katubi − *Department of Chemistry, College of Science, Princess Nourah bint Abdulrahman University, Riyadh 11671, Saudi Arabia*

Mona Saad Binkadem − *Department of Chemistry, College of Science, University of Jeddah, Jeddah 21589, Saudi Arabia*

Soha Talal Al-Goul − *Department of Chemistry, College of Sciences & Arts, King Abdulaziz University, Rabigh 21911, Saudi Arabia*

Complete contact information is available at:
https://pubs.acs.org/10.1021/acsomega.3c05882

Author Contributions

This work has been done by all authors.

Notes

The authors declare no competing financial interest.

REFERENCES

(1) Oyedotun, K. O.; et al. Advances in supercapacitor development: Materials, processes, and applications. *J. Electron. Mater.* **2023**, *52* (1), 96−129.

(2) Yadlapalli, R. T.; et al. Super capacitors for energy storage: Progress, applications and challenges. *J. Energy Storage* **2022**, *49*, No. 104194.

(3) Shah, M. Z. U.; et al. Iron-selenide-based titanium dioxide nanocomposites as a novel electrode material for asymmetric supercapacitors operating at 2.3 V. *Nanoscale Adv.* **2023**, *5* (5), 1465−1477.

(4) Lemian, D.; Bode, F. Battery-Supercapacitor Energy Storage Systems for Electrical Vehicles: A Review. *Energies* **2022**, *15* (15), 5683.

(5) Pershaanaa, M.; et al. Every bite of Supercap: A brief review on construction and enhancement of supercapacitor. *J. Energy Storage* **2022**, *50*, No. 104599.

(6) Babu, R. S.; et al. Asymmetric supercapacitor based on carbon nanofibers as the anode and two-dimensional copper cobalt oxide nanosheets as the cathode. *Chem. Eng. J.* **2019**, *366*, 390−403.

(7) Iqbal, M. Z.; Aziz, U. Supercapattery: Merging of battery-supercapacitor electrodes for hybrid energy storage devices. *J. Energy Storage* **2022**, *46*, No. 103823.

(8) Gao, Y.; Zhao, L. Review on recent advances in nanostructured transition-metal-sulfide-based electrode materials for cathode materials of asymmetric supercapacitors. *Chem. Eng. J.* **2022**, *430*, No. 132745.

(9) Imran, M.; et al. Manganese (Sulfide/Oxide) based electrode materials advancement in supercapattery devices. *Mater. Sci. Semicond. Process.* **2023**, *158*, No. 107366.

(10) Rahimi, M.; Abbaspour-Fard, M. H.; Rohani, A. Synergetic effect of N/O functional groups and microstructures of activated

carbon on supercapacitor performance by machine learning. *J. Power Sources* **2022**, *521*, No. 230968.

(11) Sun, B.; et al. Interface modification based on MnO2@ N-doped activated carbon composites for flexible solid-state asymmetric supercapacitors. *Energy* **2022**, *249*, No. 123659.

(12) dos Santos, R. D. S.; et al. High-performance asymmetric supercapacitors utilizing manganese oxide nanoparticles grafted graphitic carbon nitride nanosheets as the cathode and hypercross-linked polymer derived activated carbon as the anode. *Diamond Relat. Mater.* **2023**, *136*, No. 110005.

(13) Luo, L.; et al. A review on biomass-derived activated carbon as electrode materials for energy storage supercapacitors. *J. Energy Storage* **2022**, *55*, No. 105839.

(14) Liao, Z.; et al. Graphene aerogel with excellent property prepared by doping activated carbon and CNF for free-binder supercapacitor. *Carbohydr. Polym.* **2022**, *286*, No. 119287.

(15) Ahn, K.-S.; et al. A high-performance asymmetric super-capacitor consists of binder free electrode materials of bimetallic hydrogen phosphate (MnCo (HPO4)) hexagonal tubes and graphene ink. *Electrochim. Acta* **2022**, *426*, No. 140763.

(16) Xiong, S.; et al. Preparation of hierarchical porous activated carbons for high performance supercapacitors from coal gasification fine slag. *J. Mater. Sci.: Mater. Electron.* **2022**, *33* (18), 14722−14734.

(17) Jiang, G.; et al. Recent progress on porous carbon and its derivatives from plants as advanced electrode materials for super-capacitors. *J. Power Sources* **2022**, *520*, No. 230886.

(18) Guo, N.; et al. Enzymatic hydrolysis lignin derived hierarchical porous carbon for supercapacitors in ionic liquids with high power and energy densities. *Green Chem.* **2017**, *19* (11), 2595−2602.

(19) Xie, L.; et al. Hierarchical porous carbon microtubes derived from willow catkins for supercapacitor applications. *J. Mater. Chem. A* **2016**, *4* (5), 1637−1646.

(20) Zhang, X.; et al. GO-induced assembly of gelatin toward stacked layer-like porous carbon for advanced supercapacitors. *Nanoscale* **2016**, *8* (4), 2418−2427.

(21) Song, Y.; et al. In-situ synthesis of graphene/nitrogen-doped ordered mesoporous carbon nanosheet for supercapacitor application. *Carbon* **2016**, *96*, 955−964.

(22) Fu, H.; et al. Single layers of MoS2/Graphene nanosheets embedded in activated carbon nanofibers for high-performance supercapacitor. *J. Alloys Compd.* **2020**, *829*, No. 154557.

(23) Senokos, E.; Marcilla, R.; Vilatela, J. J. Materials science of multifunctional supercapacitors based on nanocarbon networks. In *Carbon Based Nanomaterials for Advanced Thermal and Electrochemical Energy Storage and Conversion*; Elsevier, 2019; pp 249−278.

(24) Qing, Y.; et al. Boosting the supercapacitor performance of activated carbon by constructing overall conductive networks using graphene quantum dots. *J. Mater. Chem. A* **2019**, *7* (11), 6021−6027.

(25) Mahajan, M. R.; Patil, P. O. Design of zero-dimensional graphene quantum dots based nanostructures for the detection of organophosphorus pesticides in food and water: A review. *Inorg. Chem. Commun.* **2022**, *144*, No. 109883.

(26) Luo, J.; et al. Graphene quantum dots encapsulated tremella-like NiCo2O4 for advanced asymmetric supercapacitors. *Carbon* **2019**, *146*, 1−8.

(27) Luo, P.; et al. Hydrothermal synthesis of graphene quantum dots supported on three-dimensional graphene for supercapacitors. *Nanomaterials* **2019**, *9* (2), 201.

(28) Kharangarh, P. R.; et al. Graphene quantum dots decorated on spinel nickel cobaltite nanocomposites for boosting supercapacitor electrode material performance. *J. Alloys Compd.* **2021**, *876*, No. 159990.

(29) Shen, B.; et al. Engineering the electrochemical capacitive properties of microsupercapacitors based on graphene quantum dots/MnO2 using ionic liquid gel electrolytes. *ACS Appl. Mater. Interfaces* **2015**, *7* (45), 25378−25389.

(30) Ganganboina, A. B.; Dutta Chowdhury, A.; Doong, R.-A. New avenue for appendage of graphene quantum dots on halloysite

nanotubes as anode materials for high performance supercapacitors. *ACS Sustainable Chem. Eng.* **2017**, *5* (6), 4930−4940.

(31) Wei, J. S.; et al. Carbon dots/NiCo2O4 nanocomposites with various morphologies for high performance supercapacitors. *Small* **2016**, *12* (43), 5927−5934.

(32) Zhang, X.; et al. Design and preparation of a ternary composite of graphene oxide/carbon dots/polypyrrole for supercapacitor application: Importance and unique role of carbon dots. *Carbon* **2017**, *115*, 134−146.

(33) Goswami, L. A critical review on prospects of bio-refinery products from second and third generation biomasses *Chem. Eng. J.* **2022**, *448*, 137677, DOI: 10.1016/j.cej.2022.137677.

(34) Mehta, S.; Jha, S.; Liang, H. Lignocellulose materials for supercapacitor and battery electrodes: A review. *Renewable Sustainable Energy Rev.* **2020**, *134*, No. 110345.

(35) Shoueir, K.; Mohanty, A.; Janowska, I. Industrial molasses waste in the performant synthesis of few-layer graphene and its Au/Ag nanoparticles nanocomposites. Photocatalytic and supercapacitance applications. *J. Clean. Prod.* **2022**, *351*, No. 131540.

(36) Mohlala, L. M.; et al. Beneficiation of corncob and sugarcane bagasse for energy generation and materials development in Nigeria and South Africa: A short overview. *Alexandria Eng. J.* **2016**, *55* (3), 3025−3036.

(37) Gupta, C. K.; Sachan, A.; Kumar, R. Utilization of sugarcane bagasse ash in mortar and concrete: A review *Mater. Today: Proc.* **2022**, *65*, 798−807, DOI: 10.1016/j.matpr.2022.03.304.

(38) Liu, B. Application and prospect of organic acid pretreatment in lignocellulosic biomass separation: A review *Int. J. Biol. Macromol.* **2022**, *222*, 1400−1413, DOI: 10.1016/j.ijbiomac.2022.09.270.

(39) Zhang, M.; et al. Biomass-Derived sustainable carbon materials in energy conversion and storage applications: Status and opportunities. A mini review. *Electrochem. Commun.* **2022**, *138*, No. 107283.

(40) Chai, X.; et al. A hydrothermal-carbonization process for simultaneously production of sugars, graphene quantum dots, and porous carbon from sugarcane bagasse. *Bioresour. Technol.* **2019**, *282*, 142−147.

(41) Baweja, H.; Jeet, K. Economical and green synthesis of graphene and carbon quantum dots from agricultural waste. *Mater. Res. Express* **2019**, *6* (8), No. 0850g8.

(42) Keshk, A. A.; et al. Kappa-carrageenan for benign preparation of CdSeNPs enhancing the electrochemical measurement of AC symmetric supercapacitor device based on neutral aqueous electrolyte. *Int. J. Biol. Macromol.* **2023**, *234*, No. 123620.

(43) Al Jahdaly, B. A.; et al. Phytosynthesis of Co3O4 nanoparticles as the high energy storage material of an activated carbon/Co3O4 symmetric supercapacitor device with excellent cyclic stability based on a Na2SO4 aqueous electrolyte. *ACS Omega* **2022**, *7* (27), 23673−23684.

(44) Takemura, K.; et al. Versatility of a localized surface plasmon resonance-based gold nanoparticle-alloyed quantum dot nanobiosensor for immunofluorescence detection of viruses. *Biosens. Bioelectron.* **2017**, *89*, 998−1005.

(45) Dejpasand, M. T.; et al. Tuning HOMO and LUMO of three region (UV, Vis and IR) photoluminescent nitrogen doped graphene quantum dots for photodegradation of methylene blue. *Mater. Res. Bull.* **2020**, *128*, No. 110886.

(46) Danial, W. H.; et al. The valorisation of grass waste for the green synthesis of graphene quantum dots for nonlinear optical applications. *Opt. Mater.* **2022**, *132*, No. 112853.

(47) Rashid, S.; et al. Graphene quantum dots (GQDs) decorated Co-Zn ferrite: Structural, morphological, dielectric, and magnetic properties. *J. Magn. Magn. Mater.* **2023**, *570*, No. 170548.

(48) Tayyebi, A.; et al. Supercritical water in top-down formation of tunable-sized graphene quantum dots applicable in effective photo-thermal treatments of tissues. *Carbon* **2018**, *130*, 267−272.

(49) Rathore, H. K.; et al. Charge storage mechanism in vanadium telluride/carbon nanobelts as electroactive material in an aqueous

asymmetric supercapacitor. *J. Colloid Interface Sci.* **2022**, *621*, 110−118.

(50) Abdel-Salam, A. I.; et al. Facile one-step hydrothermal method for NiCo2S4/rGO nanocomposite synthesis for efficient hybrid supercapacitor electrodes. *Mater. Chem. Phys.* **2022**, *277*, No. 125554.

(51) Li, Z.; et al. Facile strategy for preparing the composite of MoS2 microspheres and N/S dual-doped graphene stabilized by graphene quantum dots for all-solid-state asymmetric supercapacitor. *J. Alloys Compd.* **2022**, *894*, No. 162492.

(52) Cao, S.; et al. NiS/activated carbon composite derived from sodium lignosulfonate for long cycle-life asymmetric supercapacitors. *J. Alloys Compd.* **2022**, *900*, No. 163546.

(53) Zhu, H.; et al. Coupling of graphene quantum dots with MnO2 nanosheets for boosting capacitive storage in ionic liquid electrolyte. *Chem. Eng. J.* **2022**, *437*, No. 135301.

(54) Raja, T. A.; et al. Ultrasonicated graphene quantum dots dispersoid zinc ammonium phosphate hybrid electrode for supercapacitor applications. *J. Mater. Sci.: Mater. Electron.* **2022**, *33* (9), 7079−7098.

(55) Reghunath, B. S.; et al. Fabrication of bismuth ferrite/graphitic carbon nitride/N-doped graphene quantum dots composite for high performance supercapacitors. *J. Phys. Chem. Solids* **2022**, *171*, No. 110985.

(56) Zhang, C.; et al. Enhanced interfacial electron transfer by constructing NiCo-LDH hollow nanocages decorated N-doped graphene quantum dots heterojunction for high-performance supercapacitors. *Appl. Surf. Sci.* **2022**, *602*, No. 154352.

(57) Tagsin, P.; et al. Electrochemical mechanisms of activated carbon, α-MnO2 and composited activated carbon-α-MnO2 films in supercapacitor applications. *Appl. Surf. Sci.* **2021**, *570*, No. 151056.

(58) Zheng, J.; et al. One-step preparation of Ni3S4 quantum dots composite graphene/carbon nanotube conductive network for asymmetric supercapacitor. *J. Alloys Compd.* **2021**, *859*, No. 158247.